Microelectronics Reliability 176 (2026) 115985

Contents lists available at ScienceDirect

Microelectronics Reliability

journal homepage: www.elsevier.com/locate/microrel

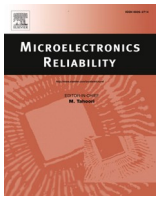

Research paper

HfO_2 barrier layers: Thickness-dependent corrosion protection of copper thin films for potential microelectronic applications with sweat contact

Osman KAHVECİ [a,d], Muh RUSDI [b], Abdullah AKKAYA [c,*], Enise AYYILDIZ [a]

[a] Department of Physics, Faculty of Science, Erciyes University, 38039, Kayseri, Türkiye
[b] Graduate School of Natural and Applied Sciences, Physics Program, Erciyes University, 38039, Kayseri, Türkiye
[c] Mucur Technical Vocational Schools, Tech. Prog. Department, Ahi Evran University, 40500, Kırşehir, Türkiye
[d] Erciyes University Energy Conversion Research and Application Center, Kayseri, Türkiye

ARTICLE INFO

Keywords:
Corrosion
Hafnium dioxide (HfO_2)
RF magnetron sputtering
Contact angle
EIS
Microelectronic devices

ABSTRACT

Copper conductive thin films or components in microelectronic devices face significant corrosion challenges that compromise long-term reliability. This study presents a comprehensive investigation of hafnium dioxide (HfO_2) as a protective barrier layer deposited by RF magnetron sputtering at varying thicknesses (150 and 300 nm) on copper substrates for possible microelectronic applications. Multi-technique characterization methods, including SEM-EDX, AFM, XRD, FTIR, UV–Vis spectroscopy, contact angle measurements, potentiodynamic polarization, and electrochemical impedance spectroscopy (EIS), were employed to establish structure, property, and performance relationships. EDX results show that the addition of an HfO_2 layer significantly modified the surface morphology, especially on presence of 300 nm HfO_2 layer, so that the surface appears continuous and uniform. This is also supported by the FTIR analysis results, which indicate the presence of the strongest Hf—O and Hf-O-Hf vibrational bonds, thereby confirming the formation of an HfO_2 layer on the Cu surface. AFM results show an increase in surface topography roughness, caused by island-type growth (Volmer-Weber), as the thickness of the HfO_2 layer increases. The XRD results for un-coated sample shows sharp and clear diffraction peaks and indicates face-centered cubic (FCC) phase pattern of pure Cu nanoparticles. When the HfO_2 layer added Cu layer, XRD pattern shows the formation of a broad hump in the range of $2\theta \approx 28°–35°$ and HfO_2 layer formed is in the amorphous state. These results are correlated with the contact angle test results. UV–Vis results show that 300 nm HfO_2 coted films has the highest transmittance value across the entire wavelength range, as well as the lowest absorbance value. The 300 nm HfO_2 coating demonstrated optimal corrosion protection with 21.2 % reduction in corrosion current density (from 11.3 to 8.89 $\mu A/cm^2$) and 29 % increase in polarization resistance (from 1.45 to 1.87 $k\Omega\ cm^2$) in artificial sweat environment. Finally, surface wettability studies revealed that increased hydrophobicity (contact angle:49.13° to 57.99°) was correlated with enhanced corrosion barrier performance. These findings establish RF-sputtered HfO_2 as a viable, scalable solution for copper protection in next-generation microelectronic and wearable biosensor applications.

1. Introduction

Thin films with thicknesses ranging from nanometers to micrometers play an important role in modern device structures [1–3]. The ability to miniaturize thin films, control their surface properties, and enable the integration of multi-layer devices makes them important components in many microelectronic applications such as sensors, integrated circuits, memories, microprocessors, and IoT devices [3–10]. In recent years, rapid developments, especially in wearable sensor technology, have further emphasized the importance of using thin-film-based materials. Sensor applications that monitor health, track physical activity, and record biological data from users require surfaces that are flexible, chemically stable, and corrosion-resistant [11–15]. Thus, the selection of materials for the development of microelectronic devices plays an important role in determining efficiency, performance, and long-term reliability [16,17].

The effort in miniaturization studies of microelectronic devices requires materials that combine superior electrical performance with high reliability under increasingly challenging operational environments [1,2]. In such a case, copper has emerged as the dominant

* Corresponding author.
E-mail address: abdullah.akkaya@ahievran.edu.tr (A. AKKAYA).

https://doi.org/10.1016/j.microrel.2025.115985
Received 7 November 2025; Received in revised form 29 November 2025; Accepted 12 December 2025
Available online 16 December 2025

interconnection material in ultra-large-scale integration (ULSI) technology, because it has high electrical conductivity, a higher melting point, resistance to electron migration, and better thermal stability compared to alternatives such as aluminum, which was previously widely used in electronic devices [15,18–21]. Copper interconnection materials also offers very low electrical resistivity of 1.68×10^{-8} Ωm. This value is approximately 40 % lower than that of aluminum, and it has superior electromigration resistance at current densities exceeding 10^6 A/cm^2 [3,21]. In addition to all these features, copper's thermodynamic instability in atmospheric conditions, particularly in the presence of moisture, chloride ions, and organic acids, reveals critical reliability challenges [21,22]. As a result, microelectronic devices such as wearable biosensors come into direct contact with skin containing sweat, which can accelerate the rate of corrosion, leading to increased electrical resistance, degradation of contact areas, and reduced long-term device reliability [17,23]. The emergence of wearable biosensors and flexible electronic devices has introduced additional corrosion challenges. These devices usually operate in direct contact with human skin, exposing them to sweat containing chloride ions (5–100 mM), lactic acid (5–40 mM), and varying acidic pH levels (4.5–7.0), present in the harsh chemical environment [23,24]. The failure mechanisms in such conditions include pitting corrosion, stress corrosion cracking, and galvanic corrosion at dissimilar metal interfaces [23,25]. The development of devices and sensor systems further emphasizes the need for reliable interconnect materials that can withstand harsh environmental conditions while maintaining application integrity [10,26].

One way to overcome this problem is to apply a protective coating using metal oxides. Metal oxides such as Al_2O_3, TiO_2, ZnO, ZrO_2, La_2O_3, SrO, Y_2O_3, and HfO_2 have been reported to be effective in improving stability and corrosion resistance [23,27–29]. Among these materials, HfO_2 stands out due to its unique optical, electrical, and chemical properties, such as high dielectric constant (~25), wide band gap, good thermal stability, resistance to chemical degradation, and optical transparency [27,28,30]. Previous research conducted by Daubert et al. [28] showed that HfO_2 is better at inhibiting the oxidation process compared to Al_2O_3. HfO_2 is also able to maintain the quality of its protective layer under long-term operating conditions. Spajic et al. [30] also found that HfO_2 exhibits better and more stable protective properties compared to Al_2O_3. Similarly, Li et al. [29] also reported that HfO_2 provides better corrosion protection performance on 304 stainless steel substrates compared to TiO_2 and ZrO_2.

In addition to the coating material, the deposition method used plays an important role in the protective ability of films [17]. Various deposition methods have been used for growth of corrosion protection materials, such as atomic layer deposition (ALD) [18,28,30], pulsed laser deposition (PLD) [31,32], electron beam evaporation [33], and RF and DC magnetron sputtering methods [18,20,34,35]. In this study, a thin copper layer was coated with HfO_2 using the RF magnetron sputtering method. This method was chosen because RF magnetron sputtering offers many advantages, including precision deposition rates, low substrate temperatures (below 200 °C), and compatibility with existing semiconductor manufacturing infrastructure [15,16]. The sputtering technique also enables precise control over film stoichiometry, density, and microstructure through optimization of sputtering parameters, including RF power, background pressure, and target-substrate distance [36,37]. This method can produce a uniform layer thickness with high adhesion and can be performed at low temperatures, thereby preventing damage to the copper substrate or interconnections.

HfO_2 possesses a unique combination of properties ideal for corrosion-protective applications due to its high dielectric constant, wide bandgap (5.5–5.7 eV), exceptional thermal stability (melting point: 2900 °C), and chemical inertness across all pH levels [35,38]. HfO_2 exhibits multiple polymorphs, including monoclinic, tetragonal, and cubic phases. These phases are dependent on deposition temperature, pressure, annealing conditions and film thickness [36,39,40]. Previous studies have explored various approaches to enhance the properties HfO_2 films. Spajić et al. [30] investigated the effect of surface preparation on Al_2O_3 and HfO_2 thin films deposited on titanium substrates, finding that HfO_2 exhibited good adhesion properties and chemical stability. Akkaya et al. [36] demonstrated that co-sputtering can modify HfO_2 properties through Ni doping, showing that post-annealing transforms films from amorphous to polycrystalline structure with reduced conductivity. Mańkowska et al. [35] showed that continuous magnetron sputtering produces superior barrier properties compared to sequential deposition, achieving corrosion current densities as low as 0.089 μA/cm^2 in NaCl solutions. Despite these advances, systematic studies correlating HfO_2 thickness with corrosion protection efficiency in physiologically relevant environments remain limited. This work addresses this gap through a comprehensive characterization of RF-sputtered HfO_2 films (150 and 300 nm) on copper, establishing quantitative structure-property-performance relationships essential for optimizing barrier layer design in next-generation skin-contact microelectronic devices.

To assess the effect of HfO_2 thickness on structural, morphological, optical, and electrochemical properties, various characterizations were performed, including scanning electron microscopy (SEM) and energy dispersive X-ray spectroscopy (EDX) for morphological and elemental composition analysis, atomic force microscopy (AFM) for surface topography, X-ray diffraction (XRD) for crystal structure, and Fourier transform infrared spectroscopy (FT-IR) and UV–Vis spectroscopy for optical properties and chemical bonding. In addition, contact angle measurements were used to evaluate surface wettability properties, and electrochemical measurements to analyze corrosion resistance using polarization test and electrochemical impedance spectroscopy (EIS). With this approach, this research providing a more comprehensive understanding of the effect of the HfO_2 layer on the corrosion resistance of copper and its potential application in improving the reliability of next-generation microelectronic devices.

2. Experimental

2.1. Materials and thin film synthesis

In order to characterize thin HfO_2 films grown on copper layers reliably, it is necessary to remove any contaminants on the glass substrate surface during the thin film deposition process. Glass substrates were cleaned in an ultrasonic cleaner with acetone, methanol, and isopropanol for 5 min each for cleaning of organic contaminations. After that, the substrates were rinsed deionized water (18 MΩ) in an ultrasonic cleaner for 5 min. Then, it was dipped in a 10 % HCl solution and subsequently, it was rinsed again with deionized water in an ultrasonic cleaner.

Cleaned glass substrates were placed in the NANOVAK NVTS-400 for the deposition process. In the first stage of deposition, a thin, conductive copper film was deposited on substrates using the DC sputtering method. The thickness of the copper film was 100 nm, and it was measured using a QCM thickness monitor. The copper target used has a purity level of 99.999 %, deposited under a flow of 5 N purity argon, with a sputtering power of 15 W and a base pressure of 10 mTorr. In the second stage, HfO_2 layers with different thicknesses (150 and 300 nm) were deposited on top of the copper film using the RF sputtering method under a flow of 5 N purity argon gas and an RF power of 100 W. The HfO_2 target powder used had a purity of 99.95 %. A schematic representation of the samples coated with HFO_2 at different thicknesses is shown in Fig. 1.

Here, work has been carried out for two different thickness values of HfO_2. When selecting this thickness, it is necessary to firstly considered the minimum thickness at which the 3D island formation process is completed in Volmer-Weber-type growth and the islands begin to coalesce (discussed in the AFM results in the "Morphological Evolution and Elemental Analysis" section). At the end of this process, continuous film formation is only completed (with the increasing thickness). Secondly, corrosion resistance can only be optimized above a certain thickness

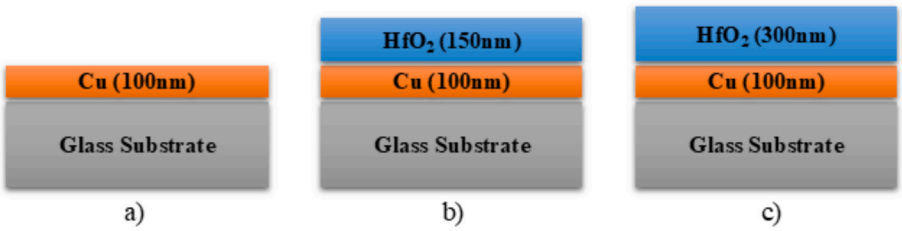

Fig. 1. Schematic representation of a) uncoated Cu thin film (C0) b) Cu thin film coated with 150 nm HfO_2 (C150), c) Cu thin film coated with 300 nm HfO_2 (C300).

(discussed in the "Polarization test" results). Therefore, in addition to the 100 nm Cu-coated (C0) sample, two samples with different coating thicknesses, 150 nm (C150) and 300 nm (C300) HfO_2 coated, were fabricated.

2.2. Characterization techniques

Surface morphology of Cu thin films and HfO_2 coated films was analyzed using scanning electron microscopy (SEM) employing Zeiss Gemini 500 and Zeiss EVO LS10 systems. High-resolution imaging was performed at an accelerating voltage of 25 kV. Energy-dispersive X-ray spectroscopy (EDX) using EDAX Inc. system provided elemental composition with a spatial resolution of approximately 1 μm. Mapping analysis was conducted over 500 × 500 μm^2 areas to verify compositional uniformity.

Atomic force microscopy (AFM) measurements were performed using a Veeco Multimode 8 system operating in tapping mode to minimize tip-sample interactions. 2D and 3D images were recorded over multiple scan area 1 × 1 μm^2, and the average surface roughness parameters, including root mean square roughness (RMS), average roughness (Ra), and ten-point height (Sz) were determined using NanoScope 3D Analysis software at a scanning area of 10 × 10 μm.

Crystal structure and phase composition were determined using X-ray diffraction (XRD) with a PANalytical Empyrean diffractometer equipped with Cu-Kα radiation source (λ = 1.5406 Å, 45 kV, 40 mA). Phase identification was performed by comparison with the JCPDS database patterns. Fourier transform infrared (FTIR) spectroscopy was conducted using a PerkinElmer 400 FT-IR/FT-FIR Spectrometer with Spotlight 400 Imaging System. Transmission mode measurements performed in the 400–4000 cm^{-1} range with 4 cm^{-1} resolution. UV–Vis spectroscopy measurements were performed using a PerkinElmer Lambda 25 spectrophotometer between 190 and 1100 nm with 1 nm resolution. Static and dynamic contact angle measurements were conducted using distilled water. Measurements employed a Biolin Scientific Attension ThetaLite 101 goniometer with a high-speed camera. Droplet volume was fixed at 2 μL with automated dispensing.

Electrochemical characterization was performed using a Wonatech Zive SP1 potentiostat/galvanostat device. A conventional three-electrode configuration was employed in a custom-made corrosion cell with 100 mL electrolyte capacity. The working electrode consisted of coated samples with a 1 cm^2 exposed area precisely defined by a chemically resistant sealant. The counter electrode was a platinum wire that ensured uniform current distribution, and an Ag/AgCl (3 M NaCl) reference electrode was used as a stable potential reference.

3. 3. Results and discussion

3.1. Morphological evolution and elemental analysis

Figs. 2a-c show FE-SEM images of uncoated and HfO_2 coated samples. In Fig. 2a (uncoated Cu films, C0), the surface typically exhibits a polycrystalline and rough morphology suitable for metallic copper films deposited by the sputter method and indicates Wolmer-Weber type growth process. A smoother surface indicates less roughness and the absence of an oxide layer. Cu grains are interlocking, but micro- to nano-voids may exist between them. Uncoated Cu metal surfaces are susceptible to preferential metallic corrosion through mechanisms such as intergranular corrosion and crack formation [17,41,42]. Uncoated Cu films are generally prone to surface oxidation and void formation at grain boundaries. This can cause variations in electrical conductivity and instability on the surface.

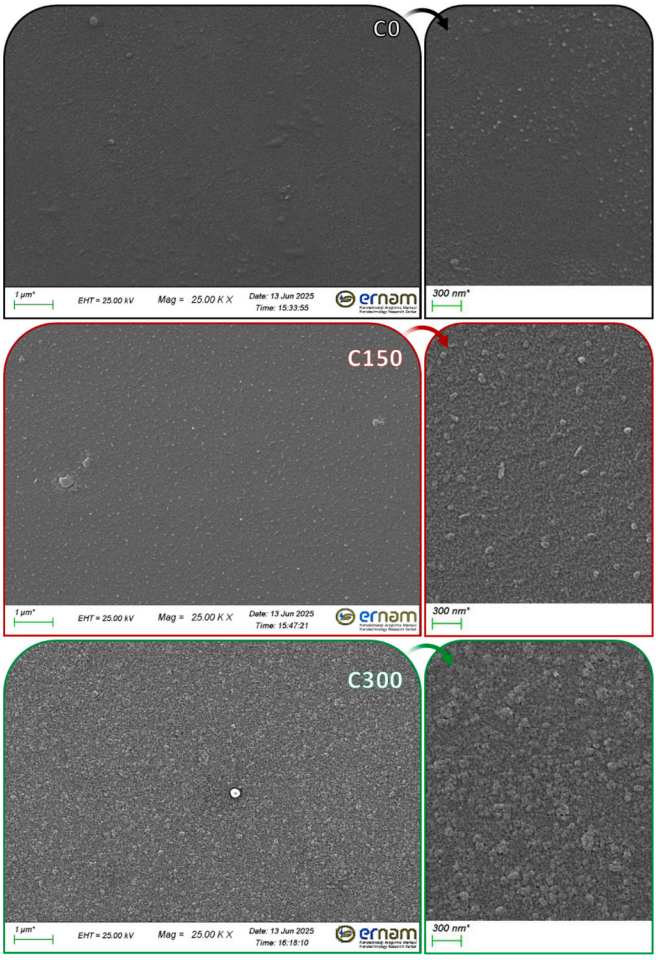

Fig. 2. FE-SEM images of a) uncoated Cu thin film, b) Cu thin film coated with 150 nm HfO_2, c) Cu thin film coated with 300 nm HfO_2.

In Fig. 2b (sample C150), oxide deposition has begun on the surface, and the surface morphology is more complex. Although the HfO_2 coating covers the Cu surface, the stable structure of a complete oxide layer is not observed. Bulge-like HfO_2 growth was observed in some areas, suggesting incomplete coalescence at this thickness. This transitional morphology indicates that the film is in the percolation threshold regime, where isolated islands begin to coalesce to form a continuous network. The HfO_2 coating partially stabilized the Cu surface,

significantly changing the film's morphology. The island-derived bulges partially increased the surface's porosity and improved surface homogeneity.

A significant change in the film's morphology can be observed in Fig. 2c (sample C300). At this thickness, the surface of the films has a very dense, compact, and uniform morphology. The island-type HfO_2 structure seen in C150 has transformed into a denser, coated oxide film. Lightening grayscale indicates the formation of an oxide layer on the metal surface. As the average atomic number on the surface decreases with oxidation, the electron signal weakens, resulting in lighter grayscale in the image [43]. This morphology is optimal for corrosion barrier applications as it minimizes defect density, eliminates continuous diffusion pathways, prevents Cu from contacting the solution, and maximizes film integrity. Therefore, the existence of a 300 nm HfO_2 layer improved surface homogeneity, resulting in a more compact film that almost completely covered the Cu surface and maximized the oxidation/diffusion barrier effect.

Further investigation of the atomic distribution across the film surface is essential to obtain a homogeneous film. EDX mapping results for samples C0, C150, and C300 show a homogeneous distribution (Fig. 3). These data are essential for understanding the variation in thin film composition at the HfO_2 layer.

EDX compositional analysis quantified the systematic variation in elemental distribution with HfO_2 thickness (Table 1). The hafnium content increased linearly from 6.10 ± 2.57 wt% (C150) to 13.13 ± 0.25 wt% (C300). The difference in O/Hf atomic ratio could be attributed to surface hydroxylation and possible incorporation of residual water vapor during deposition.

AFM images of Cu films grown with various HfO_2 layer thicknesses are shown in Figs. 4a-c. Changes in topography and surface roughness are observed in thin films. The numerical values of the roughness parameters obtained are shown in Table 2, indicating that as the HfO_2 layer thickness increases, the surface roughness also increases. AFM

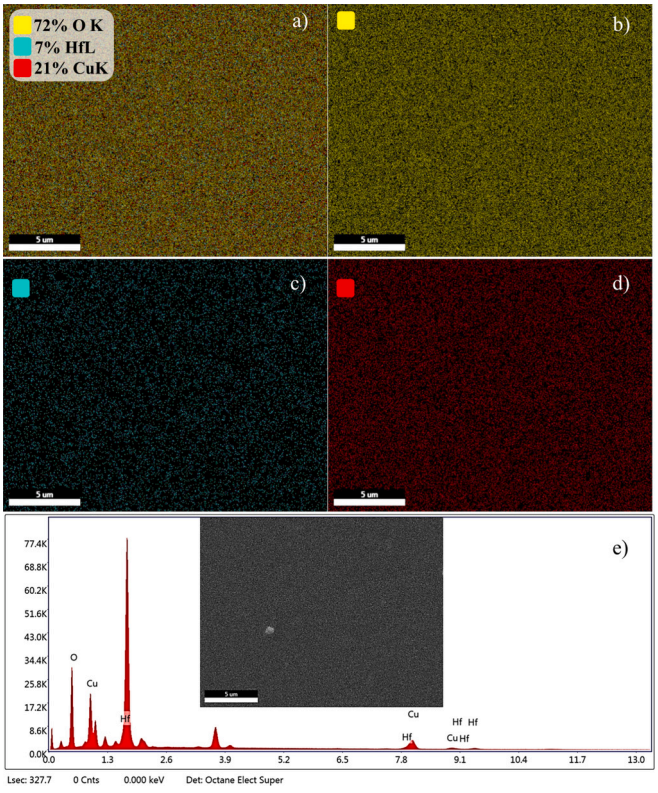

Fig. 3. EDX mapping image of the elements of thin films: a) all elements together, b) O element, c) Hf element, d) Cu element, and e) EDX peak graph taken from the image embedded in the figure.

Table 1
Elemental composition and distribution parameters from EDX analysis.

Sample Name	Elements	Weight Percentage (wt%)	Atomic Percentage (at.%)
C0	Cu	100 ± 0	100 ± 0
C150	O	61.21 ± 1.08	87.45 ± 0.01
	Hf	6.10 ± 2.57	0.79 ± 0.35
	Cu	32.70 ± 1.48	11.76 ± 0.33
C300	O	53.71 ± 0.14	84.94 ± 0.13
	Hf	13.13 ± 0.25	1.86 ± 0.03
	Cu	33.16 ± 0.40	13.20 ± 0.17

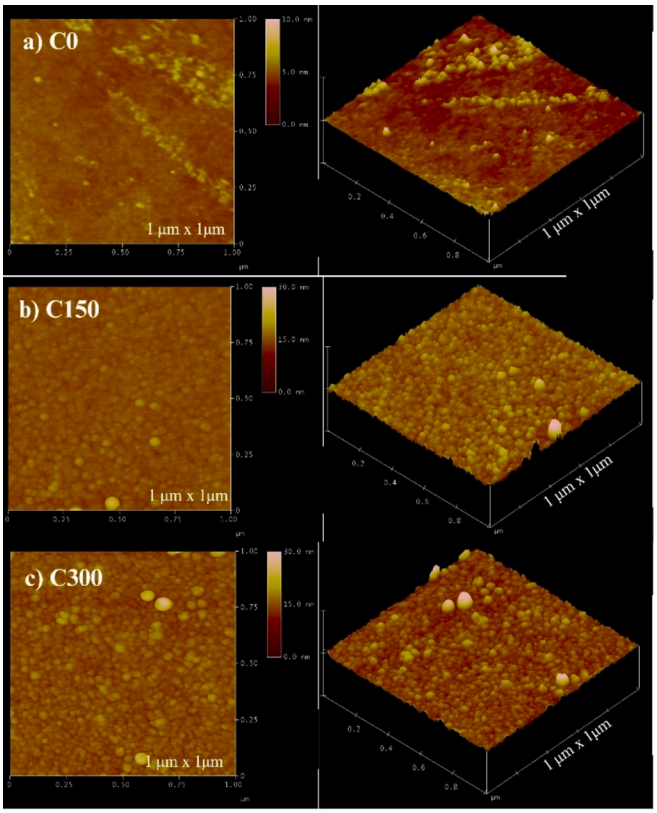

Fig. 4. 2D and 3D AFM images of thin films on a 1 × 1 µm scan area of a) C0 sample, b) C150 sample and d) C300 sample.

Table 2
Comprehensive surface roughness parameters based on AFM analysis.

Sample Name	RMS (nm)	Ra (nm)	Sz (nm)
C0	0.428	0.303	5.104
C150	0.983	0.720	14.415
C300	1.477	1.055	19.178

images depicting the topography of the film at the nanometer scale show fine waves on the film. In sample C0, the film appears to have a relatively smooth structure, with the root mean square roughness (RMS) value of 0.428 nm and average roughness (Ra) value of 0.303 nm. At this stage, topographical features begin to show local variations on the film surface. After adding the HfO_2 layer, the film topography underwent significant changes. Sample C150 showed that the film surface was completely covered by densely distributed nanosized granular structures.

The RMS, Ra, and ten-point height (Sz) values also increased to 0.983 nm, 0.720 nm, and 14.415 nm, respectively, indicating that the

film growth process began with the formation of many nucleation points which then developed into small grains. At C300, the granular structure grew larger and began to undergo grain coalescence, where small grains merged to form larger units. This is indicated by an increase in the RMS, Ra, and Sz values to 1.477 nm, 1.055 nm, and 19.178 nm, respectively. The increment in RMS value as the film thickness increases is consistent with the results reported in the literature [44–48]. Also, the systematic increase in RMS roughness from 0.428 nm (C0) to 0.983 nm (C150) to 1.477 nm (C300) follows predictable scaling laws for thin film growth.

The topographical changes observed on the film with the HfO_2 layer are consistent with the Volmer-Weber growth model. According to this model, after atoms reach the surface, they first interact with each other to form separate nucleation centers. These nucleation centers then transform into three-dimensional islands. As the growth process continues, the islands merge with each other through coalescence. Finally, as the film thickness increases, these merged islands eventually evolve into a continuous thin film morphology, completing the characteristic island-focused development stages of Volmer–Weber growth. The discrete and three-dimensional island morphology formed before the surface is completely covered at low film thicknesses causes discontinuities, voids, and local openings in the film. This situation directly affects the corrosion behavior of the films. However, as the thickness increases, the islands coalesce, resulting in a more continuous and dense film; thus, surface coverage improves, permeability decreases, and the film begins to exhibit more effective protective barrier behavior against corrosion.

So, the island growth mechanism where the interatomic bond energy (i.e., between HfO_2 adatoms) is stronger than the bond energy between the and the Cu surface [49,50]. HfO_2 don't spread evenly to form a homogeneous layer but tend to cluster to form stable islands on the Cu surface. This results in the formation of a dense granular structure and, as the thickness of the HfO_2 layer increases, these islands continue to grow and merge through grain coalesce and Ostwald ripening (i.e., the growth of large islands by consuming small islands), which ultimately leads to a significant increase in the RMS value [45,46,49,51,52].

3.2. Structural characterization and phase analysis

XRD characterization was performed to investigate the crystal structure of the prepared thin films. Fig. 5 shows the XRD patterns of the Cu thin film without coating and the Cu thin film coated with HfO_2 of different thicknesses. The XRD results for sample C0 show sharp and clear diffraction peaks. The peaks that appear are characteristic of pure Cu. The main peaks were detected at $2\theta \approx 43.6°$, 50.6°, and 74.3°, which are related to the (111), (200), and (220) planes (JCPDS No. 040836) [36,53]. All diffraction peaks are consistent with the standard face-centered cubic (FCC) phase pattern of pure Cu nanoparticles, confirming that Cu has a cubic lattice structure [46,49]. In addition, small peaks were detected at $2\theta \approx 36.5°$ (111) and 61.5° (220), indicating partial oxidation of copper, resulting in the formation of the Cu_2O phase [41]. On the other hand, a broad peak appeared in the range of $2\theta \approx 20°–30°$, which was attributed to the amorphous nature of the glass substrate.

The addition of an HfO_2 layer to the Cu thin film produces new features in the XRD pattern. The film shows the formation of a broad hump in the range of $2\theta \approx 28°–35°$. This hump appears stronger and clearer as the thickness of the HfO_2 layer increases. The absence of sharp characteristic diffraction peaks of the monoclinic phase of HfO_2 at $2\theta \approx 28.5°$ (−111), 31.6° (111), and 34.5° (002) (JCPDS No. 00–08–342) indicates that the HfO_2 layer formed is in the amorphous state. This result shows a similarity to the results reported in the literature [36,44,47,52,54,55]. This amorphous structure is highly advantageous as a diffusion barrier because, in the amorphous state, there are no grain boundaries that can serve as fast pathways for corrosion and Cu diffusion, thereby increasing its effectiveness as a protective layer [54].

FTIR characterization was performed to identify functional groups and molecular bonds resulting from the presence of the HfO_2 layer. In Fig. 6, sample C0 shows peaks associated with surface contaminants such as O—H (~3758 cm^{-1}), C—H (~2918 cm^{-1}), and CO_2 (~2297 cm^{-1}), as well as weak peaks below 1600 cm^{-1} that may be related to Cu—O or other contaminants, although not dominant. Sample C150 displays new peaks below 1000 cm^{-1} (~869, 735, 555, 473 cm^{-1}) characteristic of Hf—O and Hf–O–Hf vibrations, confirming the presence of the HfO_2 layer [47,56]. C300 shows a similar pattern with higher absorption intensities in the <1000 cm^{-1} region and is clearly visible around ~875 cm^{-1} and ~ 731 cm^{-1}, indicating that thicker layers interact more intensely with infrared radiation, resulting in lower transmission peaks. The appearance of Hf—O and Hf–O–Hf vibrations indicates that the HfO_2 layer was successfully deposited on the surface of the thin Cu film. The presence of Hf—O and Hf-O-Hf vibrations in the range below 1000 cm^{-1} shows a significant similarity to the results reported in the literature [47,56–58].

3.3. Optical properties and surface wettability

UV–Vis characterization was performed to investigate the optical properties of the films. Fig. 7a shows the transmittance spectrum, and Fig. 7b shows the absorbance spectrum. Based on the transmittance spectrum graph (Fig. 7a), sample C300 has the highest transmittance

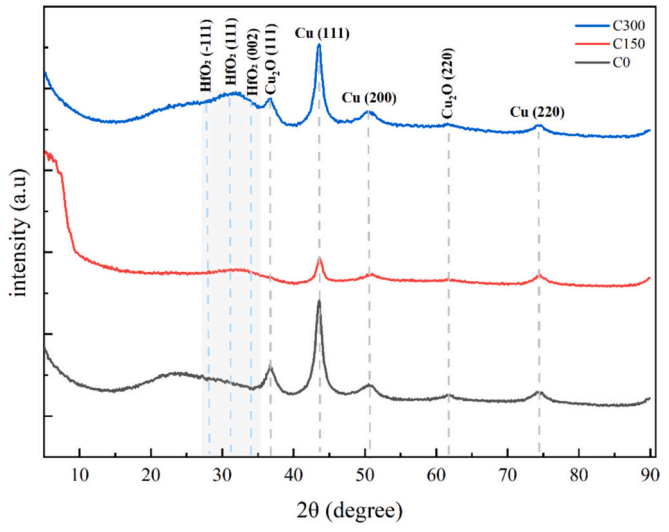

Fig. 5. XRD patterns of uncoated Cu thin film (C0), Cu thin film coated with 150 nm HfO_2 (C150) and Cu thin film coated with 300 nm HfO_2 (C300).

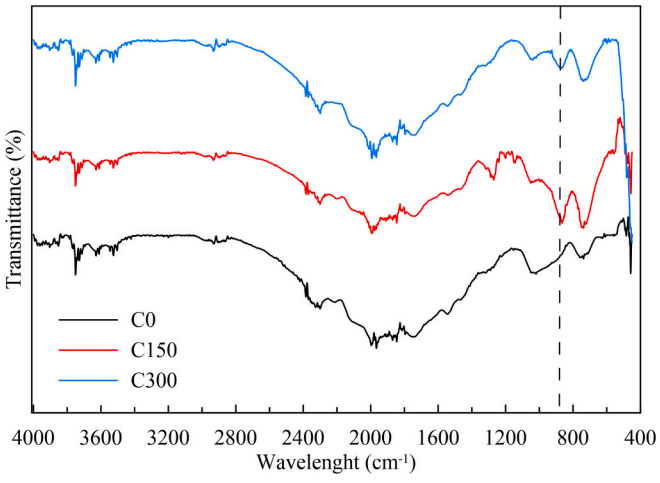

Fig. 6. FT-IR spectra of uncoated Cu and HfO_2-coated Cu thin films with thicknesses of 150 nm and 300 nm.

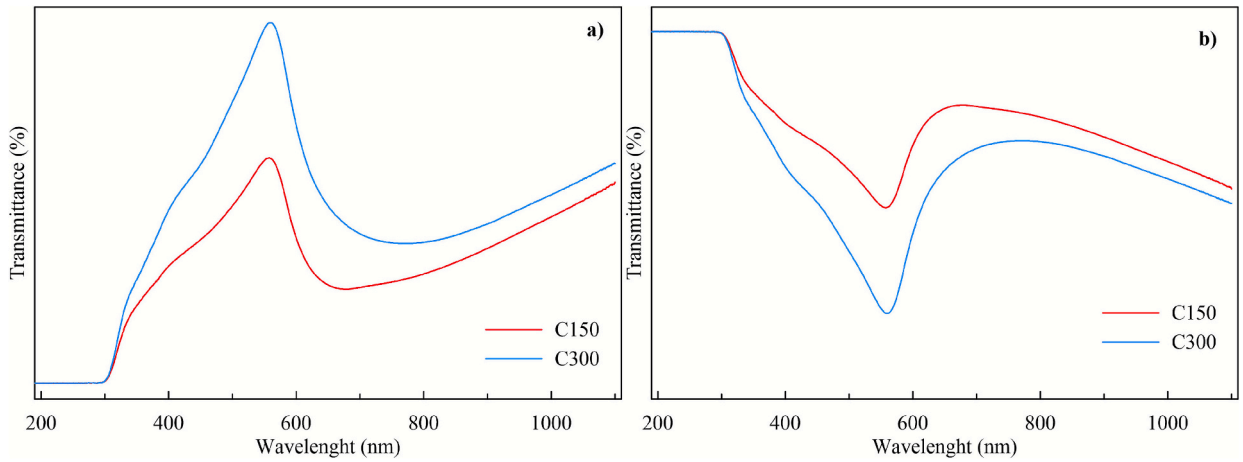

Fig. 7. UV–Vis (a) transmittance spectra and (b) absorbance spectra of uncoated Cu and HfO_2-coated Cu thin films with thicknesses of 150 nm and 300 nm.

value across the entire wavelength range compared to C0 and C150. The highest transmittance value was found at around 550 nm wavelength with a maximum value of approximately 11.5 %. The increase in transmittance value with increasing HfO_2 layer thickness indicates that HfO_2 can function as an anti-reflective coating. This is due to the transparency of HfO_2 in the visible light region and its large band gap energy, which prevents the absorption of low-energy photons below the UV limit [59–61]. However, the transmittance values for sample C150 were lower than those for C0, at 7 % and 8 %, respectively. This transmittance value is likely due to the HfO_2 layer not being thick enough, which causes greater reflection [61].

In Fig. 7b, at wavelengths <400 nm (UV region), all thin films show high absorbance values (>9 a.u.). At wavelengths >400 nm (visible light region), the absorbance values drop sharply and reach a more stable and relatively low point (around 1–2 a.u.). Sample C300 shows the lowest absorbance value, which is consistent with the transmittance results; these values are inversely proportional. The decrease in absorbance in C300 is attributed to the HfO_2 layer that blocks the interaction of light with the Cu substrate, as well as the dielectric properties of HfO_2, which can reduce excess light absorption [59,60].

The wettability of thin film surfaces was evaluated using contact angles. The contact angle measurement results are shown in Figs. 8a and 8b. In Fig. 8a, sample C0 shows flatter droplets compared to C150 and C300, indicating a smaller contact angle. The droplets on C300 appear rounder, indicating the highest contact angle compared to the other samples. Table 3 shows the numerical values of the contact angle measurements. C0 has an average contact angle (49.13 ± 2.90°), indicating the most hydrophilic surface properties. The contact angle values increased after the thin Cu film was coated with HfO_2, namely (53.32 ± 0.22°) on C150 and (57.99 ± 0.36°) on C300. All films had contact angle values below 90°, indicating that the entire surface was still hydrophilic.

The dynamic graph in Fig. 8b shows that the contact angle of C0

Table 3
Comprehensive static contact angle measurement results on the thin films surface.

Sample	Left Contact Angle (°)	Right Contact Angle (°)	Average Contact Angle (°)
C0	49.01 ± 2.81	49.26 ± 3.0	49.13 ± 2.90
C150	53.12 ± 0.23	53.52 ± 0.22	53.32 ± 0.22
C300	57.17 ± 0.21	58.81 ± 0.52	57.99 ± 0.36

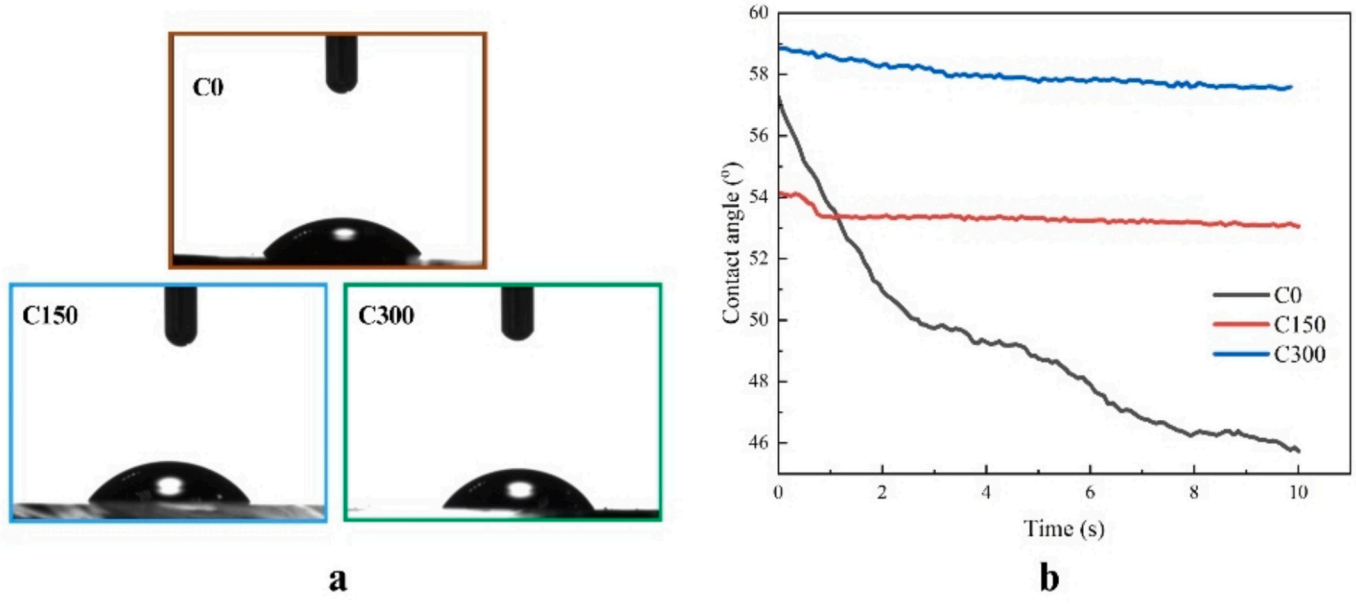

Fig. 8. (a) contact angles on different surfaces of thin films (C0, C150, C300), (b) change in contact angle over time for 10 s in the samples.

decreased gradually from approximately 57° to below 46° within 10 s. After being coated with HfO_2, the sample exhibited better stability (around 53° and 58° for C150 and C300, respectively). The average advancing contact angle increased monotonically from 49.13° (C0) to 57.99° (C300), while contact angle hysteresis (the difference between advancing and receding angles) decreased from 4.20° to 1.90° (C150), before slightly increasing to 2.10° (C300). This non-monotonic hysteresis behavior reflects competing effects: improved chemical homogeneity versus increased roughness, and is consistent with the AFM results. This phenomenon is directly related to the composition and topography of the surface; an increase in the thickness of the HfO_2 layer consistently causes a rise in the contact angle [62,63]. Additionally, the roughness of films hinders the movement of water droplet edges, making it more challenging for water to spread and resulting in a larger contact angle [62–64].

3.4. Electrochemical performance analysis

3.4.1. Polarization test

This was done to obtain the Tafel curve and evaluate the electrochemical behavior of the corrosion of Cu thin films without coating and with HfO_2 coating. Fig. 9 shows that with the addition of HfO_2 coating on the Cu thin film, the corrosion potential (E_{corr}) shifts towards a more positive value. The E_{corr} value at C0 is −200 mV, while at C150 and C300 it increases to −168 mV and − 153 mV, respectively. This positive shift indicates that the HfO_2 coating provides thermodynamic stability on the surface and effectively increase the corrosion resistance of thin Cu films [28].

The effectiveness of protection increases with the thickness of the HfO_2 layer, as shown in the results of the electrochemical parameter analysis (Table 4). The polarization resistance (Rp) value was calculated using the Stern–Geary equation [28,65]:

$$Rp = \frac{\beta_a \times \beta_c}{J_{corr} \times 2.3 \times (\beta_a + \beta_c)}$$

where βa and βc are the anodic and cathodic slopes of the Tafel curve, respectively. The corrosion rate (CR) is calculated using Eq. [65]:

$$CR\left(\frac{mm}{year}\right) = \frac{3.16 \times 10^{-2} \times J_{corr} \times EW}{D \times z \times F}$$

Where EW is the equivalent weight of the corroded metal, F is Faraday's constant, z is the number of electrons transferred per Cu atom, and D is the density of the metal (g/cm^2).

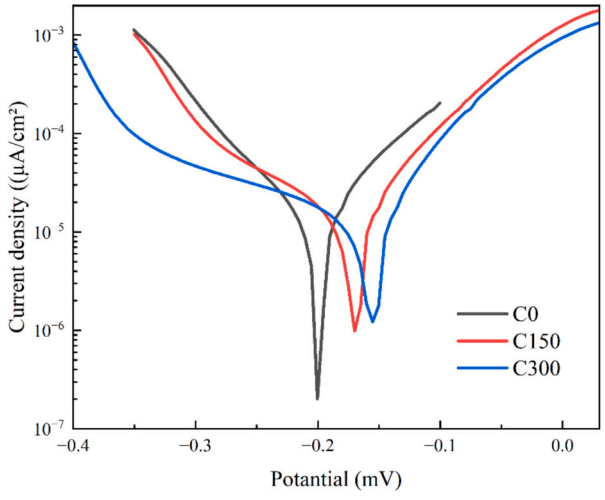

Fig. 9. Tafel curve of uncoated Cu and HfO_2-coated Cu thin films with thicknesses of 150 nm and 300 nm.

When evaluating the fit between the experimental data and the model, if we take into account that small chi-square values indicate a better fit between the model and the data, while large values indicate a lack of fit; the chi square values of the order of 10^{-11} and the R-square results indicating 98 % to 99 % fit indicate that the model is quite consistent with the experimental data.

The J_{corr} value decreases gradually as the thickness of the HfO_2 layer increases. The J_{corr} value at C0, which is 11.3 μA/cm^2, decreases to 9.59 μA/cm^2 and 8.89 μA/cm^2 at C150 and C300. The corrosion rate (CR) (mm/year) also decreased from 0.132 at C0 to 0.112 and 0.104 at C150 and C300. The polarization resistance (Rp) value, which measures the material's ability to resist the corrosion process at the interface, increased. Sample C0 had a value of 1.45 kΩ·cm^2, which increased to 1.64 kΩ·cm^2 and 1.87 kΩ·cm^2 in samples C150 and C300, respectively. According to the Stern-Geary relationship, the corrosion rate is inversely proportional to Rp. Therefore, C300 has the best corrosion resistance [28].

Table 5 primarily summarizes studies examining the behavior of copper in artificial sweat solutions, along with selected reports on HfO_2-based corrosion-protection coatings. The corrosion parameters reported for Cu show strong agreement with the results obtained in the present work. Likewise, the performance of HfO_2 barrier coatings in various electrolytes is generally consistent with the findings of this study, although minor differences may arise due to variations in the solution environment.

3.4.2. Electrochemical impedance spectroscopy

EIS testing was conducted to analyze the corrosion mechanism in uncoated Cu thin films and Cu thin films with HfO_2 coatings. Fig. 10 shows that all thin films exhibit similar patterns. At high frequencies, curves with nearly identical slopes appear, followed by semi-circular patterns at medium frequencies and then elongated tails at low frequencies. The high-frequency region is dominated by ohmic resistance [70]. Since all measurements were performed in the same electrolyte solution, no significant differences were observed in this region. The behavior in the medium- and low-frequency regions suggests the presence of charge transfer processes and contributions from the interface and diffusion [71]. C0 (uncoated Cu) exhibits more pronounced capacitive behavior and lower impedance at mid-frequencies compared to HfO_2-coated thin Cu films. The lower capacitive behavior compared to HfO_2-coated samples, along with the lower charge transfer resistance at small circle diameters along the real axis, indicates that charge transfer across the Cu surface to the artificial sweat solution occurs relatively easily. This indicates that in thin Cu films without coating, charge transfer occurs more easily, and electrochemical reactions occur more rapidly [71]. The results are consistent with the dark gray tones observed in SEM analysis (indicating low oxide presence) and the island-type oxide growths observed in AFM.

As the thickness of the HfO_2 layer increases, the imaginary impedance value increases and the semi-circular curve shape becomes wider, indicating that the interface and surface layer become more resistive and the charge transfer process occurs more slowly [72]. The slope of the tail at low frequencies decreases with increasing layer thickness, indicating that the increase in the surface layer inhibits diffusion and mass transfer [72]. Based on the results of EIS analysis, it can be concluded that C300 forms a more effective surface barrier against the test solution by slowing down charge transfer, diffusion, and mass transfer. In AFM analyses, the increase in surface roughness caused the drop to remain at a larger angle on the surface, as observed in the contact angle analyses. In the dynamic analysis of the contact angle, the lower change in angle over time in the HfO_2-coated samples is consistent with the results, indicating that the HfO_2-coated Cu surface is more resistant to corrosive environments. Thus, the HfO_2 layer on the Cu thin film can increase corrosion resistance by forming an effective diffusion barrier against artificial sweat penetration.

Table 4
Electrochemical parameters of the samples derived from Tafel polarization measurements.

Sample	βa (mV)	-βc (mV)	J_{corr} (μA cm^{-2})	E_{corr} (mV)	Rp (kΩ cm^2)	CR (mm $year^{-1}$)	χ^2 ($\times 10^{-11}$)	R^2
C0	68.7 ± 4.1	83.8 ± 4.8	11.3 ± 1.1	−200 ± 0.8	1.45	0.132	1.02	0.99
C150	54.8 ± 8.6	108 ± 16.6	9.59 ± 2.5	−168 ± 0.9	1.64	0.112	1.18	0.98
C300	50.9 ± 0.56	155 ± 18.1	8.89 ± 2.3	−153 ± 1.2	1.87	0.104	1.27	0.98

Table 5
Summary of studies evaluating the corrosion behavior of Cu in artificial sweat solutions and selected reports on HfO_2-based barrier coatings.

Sample	Exposure environment	J_{corr} (μA cm^{-2})	Rp (kΩ cm^2)	Studies
Cu Thin film	Artificial sweat	11.3	1.45	This work
Cu/HfO_2 (150 nm)	Artificial sweat	9.59	1.64	This work
Cu/HfO_2 (300 nm)	Artificial sweat	8.89	1.87	This work
Cu Coins	Artificial sweat	11.1	2.3	[66]
Bare Cu	Artificial sweat	15.48	–	[67]
BareCu	0.1 M NaCl	1.28	15	[28]
Bare Cu/HfO_2 (60 nm)	0.1 M NaCl	0.22	89	[28]
Commercial 7075 Al	Artificial sweat	57.5	–	[68]
AZ31 Mg alloy/HfO_2	body fluid	0.6	–	[69]

4. Conclusions

In this work, HfO_2 layers with thicknesses of 150 and 300 nm were deposited on Cu thin films to evaluate their thickness-dependent corrosion behavior in an artificial sweat environment. SEM–EDX and AFM analyses revealed that the 300 nm HfO_2 layer significantly improved surface homogeneity, with the hafnium content increasing from 6.10 ± 2.57 wt% (C150) to 13.13 ± 0.25 wt% (C300), accompanied by a systematic roughness increase from 0.428 nm (C0) to 1.477 nm (C300). XRD measurements confirmed the FCC Cu reflections at 43.6°, 50.6°, and 74.3°, while both coated samples exhibited a broad amorphous hump in the 28–35° range, indicating that the HfO_2 layers remained fully amorphous. FTIR spectra showing characteristic Hf—O and Hf–O–Hf vibrational modes in the fingerprint region (~869, 735, 555, 473 cm^{-1}) confirmed the incorporation of HfO_2 in both coated films. Optical spectra showed that the 300 nm coating achieved the highest transmittance (≈11.5 % around 550 nm) and the lowest absorbance across the visible region. Surface wettability also improved with increasing thickness, with the contact angle rising from 49.13° (C0) to 57.99° (C300). Electrochemical performance analysis demonstrated that the 300 nm HfO_2 coating provided the most effective corrosion protection, reducing the corrosion current density from 11.3 ± 1.1 to 8.89 ± 2.3 μA/cm^2 and increasing the polarization resistance from 1.45 to 1.87 kΩ·cm^2.

Overall, this study shows that both the RF magnetron sputtering process and the final HfO_2 layer thickness critically influence the structural and electrochemical behavior of the coatings. The findings confirm that amorphous HfO_2 films-particularly at 300 nm-serve as highly effective corrosion barriers for Cu thin films in microelectronic applications, with performance strongly governed by film thickness and morphology. Future work may focus on examining how post-annealing affects the crystallization, morphology, and corrosion performance of HfO_2 layers.

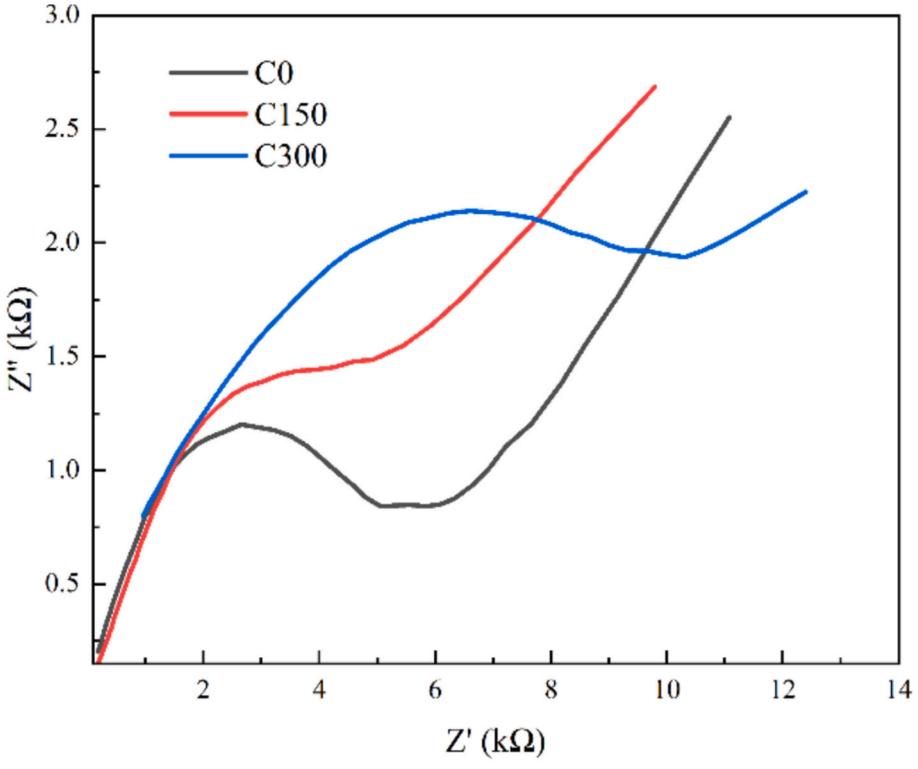

Fig. 10. Nyquist plot of EIS measurement results for uncoated Cu and HfO_2-coated thin films with thicknesses of 150 nm and 300 nm.

CRediT authorship contribution statement

Osman Kahveci: Writing – review & editing, Methodology, Methodology, Investigation, Formal analysis, Conceptualization. **Muh Rusdi:** Writing – original draft, Visualization, Formal analysis, Data curation. **Abdullah Akkaya:** Writing – original draft, Methodology, Formal analysis, Conceptualization. **Enise Ayyıldız**: Writing – review & editing, Supervision, Funding, Project administration.

Declaration of competing interest

The authors declare the following financial interests/personal relationships which may be considered as potential competing interests:

Enise AYYILDIZ reports financial support was provided by Erciyes University Scientific Research Projects Coordination Unit. If there are other authors, they declare that they have no known competing financial interests or personal relationships that could have appeared to influence the work reported in this paper.

Acknowledgments

The authors thanks to Erciyes University Scientific Research Projects Unit (Project FYL-2025-15313) for financial support.

Data availability

Data will be made available on request.

References

[1] K.L. Mittal, Adhesion measurement of thin films, Active and Passive Electronic Components 3 (1) (1976) 936912.
[2] Y. Taga, Recent progress of nanotechnologies of thin films for industrial applications, Mater. Sci. Eng. C 15 (1) (2001) 231–235.
[3] S. Sakthinathan, G.A. Meenakshi, S. Vinothini, C.-L. Yu, C.-L. Chen, T.-W. Chiu, N. Vittayakorn, A Review of thin-film growth, properties, applications, and future prospects, Processes 13 (2) (2025) 587.
[4] O. Bonnaud, The challenges of microelectronics for the future digital society: the roles of thin film technologies and of the higher education, journal of materials science and chemical Engineering 7 (2019) 47–56.
[5] J. Schmitz, Low temperature thin films for next-generation microelectronics (invited), Surf. Coat. Technol. 343 (2018) 83–88.
[6] J. Zhang, Y. Li, K. Cao, R. Chen, Advances in atomic layer deposition, Nanomanufacturing and Metrology 5 (3) (2022) 191–208.
[7] R. Garg, S. Gonuguntla, S. Sk, M.S. Iqbal, A.O. Dada, U. Pal, M. Ahmadipour, Sputtering thin films: materials, applications, challenges and future directions, Adv. Colloid Interf. Sci. 330 (2024) 103203.
[8] L. Qi, L. Kong, Y. Wang, J. Song, A. Azam, Z. Zhang, J. Yan, Recent Progress in application-oriented self-powered microelectronics, Adv. Energy Mater. 13 (47) (2023) 2302699.
[9] B. Dieny, I.L. Prejbeanu, K. Garello, P. Gambardella, P. Freitas, R. Lehndorff, W. Raberg, U. Ebels, S.O. Demokritov, J. Akerman, A. Deac, P. Pirro, C. Adelmann, A. Anane, A.V. Chumak, A. Hirohata, S. Mangin, S.O. Valenzuela, M.C. Onbaşlı, M. d'Aquino, G. Prenat, G. Finocchio, L. Lopez-Diaz, R. Chantrell, O. Chubykalo-Fesenko, P. Bortolotti, Opportunities and challenges for spintronics in the microelectronics industry, Nature Electronics 3 (8) (2020) 446–459.
[10] A. Kumar, A.K. Goyal, N. Gupta, Review—thin-film transistors (TFTs) for highly sensitive biosensing applications: a Review, Ecs J Solid State Sc 9 (11) (2020) 115022.
[11] M.J. Mirshojaeian Hosseini, R.A. Nawrocki, A Review of the Progress of thin-film transistors and their technologies for flexible electronics, Micromachines-Basel 12 (6) (2021) 655.
[12] J. Liu, H. Liu, Research on flexible sensors for wearable devices: a Review, Nanomaterials-Basel 15 (7) (2025) 520.
[13] A.J. Bandodkar, W. Jia, J. Wang, Tattoo-based wearable electrochemical devices: a Review, Electroanal 27 (3) (2015) 562–572.
[14] D. Luo, H. Sun, Q. Li, X. Niu, Y. He, H. Liu, Flexible sweat sensors: from films to textiles, ACS Sens. 8 (2) (2023) 465–481.
[15] R.K. Baruah, H. Yoo, E.K. Lee, Interconnection Technologies for Flexible Electronics: materials, fabrications, and applications, Micromachines-Basel 14 (6) (2023) 1131.
[16] K. Nyako, S. Devkota, F. Li, V. Borra, Building Trust in Microelectronics: a comprehensive Review of current techniques and adoption challenges, Electronics 12 (22) (2023) 4618.
[17] M. Abdullah, M.M. Hosain, M.M. Hassan Parvez, M.S. Haque Motayed, Prospects and challenges of thin film coating materials and their applications, Inorg. Chem. Commun. 175 (2025) 114117.
[18] R. Haeffele, S. Marcelin, L. Broussous, L. Mazet, B. Normand, Electrochemical characterization of localized corrosion mechanism of ALD Al2O3-coated copper for microelectronic application, Corros. Sci. 234 (2024) 112135.
[19] R.P. Vinci, E.M. Zielinski, J.C. Bravman, Thermal strain and stress in copper thin films, Thin Solid Films 262 (1) (1995) 142–153.
[20] B. Giroire, M. Ali Ahmad, G. Aubert, L. Teule-Gay, D. Michau, J.J. Watkins, C. Aymonier, A. Poulon-Quintin, A comparative study of copper thin films deposited using magnetron sputtering and supercritical fluid deposition techniques, Thin Solid Films 643 (2017) 53–59.
[21] T. Gupta, Copper Interconnect Technology, Springer, New York, London, 2010.
[22] D.M. Bastidas, M. Criado, S. Fajardo, V.M. La Iglesia, E. Cano, J.M. Bastidas, Copper deterioration: causes, diagnosis and risk minimisation, Int. Mater. Rev. 55 (2) (2010) 99–127.
[23] Q. Zhao, X. Liu, H. Wang, Y. Zhu, Y. An, D. Yu, J. Qi, Research Progress in corrosion protection Technology for Electronic Components, Metals 13 (9) (2023) 1508.
[24] C.J. Harvey, R.F. LeBouf, A.B. Stefaniak, Formulation and stability of a novel artificial human sweat under conditions of storage and use, Toxicol. in Vitro 24 (6) (2010) 1790–1796.
[25] L.Z. Mohamed, A.M. Elzohry, L.A. Khorshed, A. Attia, M.A. Adly, Corrosion behavior of coins in artificial sweat solution: a Review, Int J Electrochem Sc 17 (1) (2022) 220110.
[26] A.M. Elbasiony, S. Alharthi, M. Mohamady Ghobashy, W.E. Boraie, M.S. Attia, M. Madani, S. Ali Al-Gahtany, R. Darwesh, M. Shaban, A.I. Sharshir, Development and application of novel biosensors for enhanced detection in medical diagnostics, Microchem. J. 207 (2024) 111938.
[27] M. Awang, A.A. Khalili, S.R. Pedapati, A review: thin protective coating for wear protection in high-temperature application, Metals 10 (1) (2020) 42.
[28] J.S. Daubert, G.T. Hill, H.N. Gotsch, A.P. Gremaud, J.S. Ovental, P.S. Williams, C. J. Oldham, G.N. Parsons, Corrosion protection of copper using Al_2O_3, TiO_2, ZnO, HfO_2, and ZrO_2 atomic layer deposition, ACS Appl. Mater. Interfaces 9 (4) (2017) 4192–4201.
[29] M. Li, Z.-X. Jin, W. Zhang, Y.-H. Bai, Y.-Q. Cao, W.-M. Li, D. Wu, A.-D. Li, Comparison of chemical stability and corrosion resistance of group IV metal oxide films formed by thermal and plasma-enhanced atomic layer deposition, Sci Rep-Uk 9 (1) (2019) 10438.
[30] I. Spajić, P. Rodič, G. Šekularac, M. Lekka, L. Fedrizzi, I. Milošev, The effect of surface preparation on the protective properties of Al_2O_3 and HfO_2 thin films deposited on cp-titanium by atomic layer deposition, Electrochim. Acta 366 (2021) 137431.
[31] S.R. Suryawanshi, R.T. Shisode, K.K. Jagtap, D.J. Late, S.S. Suryavanshi, M. A. More, Electrical characterization of pulsed laser deposited high-k HfO_2 nanoparticles on tapered Cu_2O nanowires: promising cold cathode applications, J. Mater. Sci. Mater. Electron. 32 (7) (2021) 8440–8449.
[32] C.-L. Tien, Special issue "advanced coating technology by physical vapor deposition and applications", Coatings 13 (2) (2023) 467.
[33] S. Kant, N. Kumari, M. Kumar, Effect of deposition conditions on the morphological, optical, and corrosion behavior of electron beam evaporated high-performance HfO_2 thin films, Applied Physics A 131 (8) (2025) 631.
[34] A. Vinod, M.S. Rathore, N. Srinivasa Rao, Effects of annealing on quality and stoichiometry of HfO_2 thin films grown by RF magnetron sputtering, Vacuum 155 (2018) 339–344.
[35] E. Mańkowska, M. Mazur, M. Kalisz, M. Grobelny, J. Domaradzki, D. Wojcieszak, Characterization of structural, optical, corrosion, and mechanical properties of HfO_2 thin films deposited using pulsed DC magnetron sputtering, Materials 16 (14) (2023) 5005.
[36] A. Akkaya, O. Kahveci, B. Şahin, E. Ayyıldız, Simultaneously-doping of HfO_2 thin films by Ni with sputtering technique and effect of post annealing on structural and electrical properties, Phys. B Condens. Matter 665 (2023) 415034.
[37] H. El Aakib, N. Rochdi, A. Tchenka, J.-F. Pierson, A. Outzourhit, Copper oxide coatings deposited by reactive radio-frequency sputtering for solar absorber applications, Mater. Chem. Phys. 296 (2023) 127196.
[38] L. Staišiūnas, K. Leinartas, E. Juzeliūnas, D. Bučinskienė, A. Grigucevičienė, P. Kalinauskas, A. Selskis, S. Stanionytė, Anticorrosion performance of hafnium oxide ultrathin films on AZ31 magnesium alloy, Surf. Coat. Technol. 397 (2020) 126046.
[39] C.T. Kuo, R. Kwor, K.M. Jones, Study of sputtered HfO_2 thin films on silicon, Thin Solid Films 213 (2) (1992) 257–264.
[40] T. Mittmann, M. Materano, P.D. Lomenzo, M.H. Park, I. Stolichnov, M. Cavalieri, C. Zhou, C.-C. Chung, J.L. Jones, T. Szyjka, M. Müller, A. Kersch, T. Mikolajick, U. Schroeder, Origin of ferroelectric phase in Undoped HfO_2 films deposited by sputtering, Adv. Mater. Interfaces 6 (11) (2019) 1900042.
[41] D. Mahana, A.K. Mauraya, P. Singh, S.K. Muthusamy, Evolution of CuO thin films through thermal oxidation of cu films prepared by physical vapour deposition techniques, Solid State Commun. 366-367 (2023) 115152.
[42] U. Kamachi Mudali, J. Jayaraj, R.K.S. Raman, B. Raj, Corrosion, Non-Destructive Evaluation of Corrosion and Corrosion-assisted Cracking, 2019, pp. 56–74.
[43] J.I. Goldstein, D.E. Newbury, J.R. Michael, N.W.M. Ritchie, J.H.J. Scott, D.C. Joy, Scanning Electron Microscopy and X-Ray Microanalysis, Springer New York, 2017.
[44] J.C. Hackley, T. Gougousi, Properties of atomic layer deposited HfO_2 thin films, Thin Solid Films 517 (24) (2009) 6576–6583.
[45] L. Zhang, J. Zhang, H. Jiao, G. Bao, Z. Wang, X. Cheng, Thickness-dependent surface morphology and crystallization of HfO_2 coatings prepared with ion-assisted deposition, Thin Solid Films 642 (2017) 359–363.
[46] A. Wiatrowski, A. Obstarczyk, M. Mazur, D. Kaczmarek, D. Wojcieszak, Characterization of HfO_2 optical coatings deposited by MF magnetron sputtering, Coatings 9 (2) (2019) 106.

[47] J.d.J. Araiza, L. Álvarez-Fraga, R. Gago, O. Sánchez, Surface morphology and optical properties of hafnium oxide thin films produced by magnetron sputtering, Materials 16 (15) (2023) 5331.
[48] M. Dhanunjaya, N. Manikanthababu, S. Ojha, S. Pojprapai, A.P. Pathak, S.V. S. Nageswara Rao, Effects of growth parameters on HfO_2 thin-films deposited by RF magnetron sputtering, Radiat Eff Defect S 177 (1–2) (2022) 15–26.
[49] H.J. Park, Y.M. Sun, H. Troiani, P. Santiago, M.J. Yacaman, J.M. White, Growth and thermal annealing of cu on HfO_2, Surf. Sci. 521 (1) (2002) 1–9.
[50] U. Schroeder, M.H. Park, T. Mikolajick, C.S. Hwang, The fundamentals and applications of ferroelectric HfO_2, Nat. Rev. Mater. 7 (8) (2022) 653–669.
[51] N. Kaiser, Review of the fundamentals of thin-film growth, Appl. Opt. 41 (16) (2002) 3053–3060.
[52] S. Li, Y. Zhang, D. Yang, W. Yang, X. Chen, H. Zhao, J. Hou, P. Yang, Structure and optical properties of HfO_2 films on Si (100) substrates prepared by ALD at different temperatures, Phys. B Condens. Matter 584 (2020) 412065.
[53] V. Abhinav K, V.K. Rao R, P.S. Karthik, S.P. Singh, Copper conductive inks: synthesis and utilization in flexible electronics, RSC Adv. 5 (79) (2015) 63985–64030.
[54] M. Kotilainen, R. Krumpolec, D. Franta, P. Souček, T. Homola, D.C. Cameron, P. Vuoristo, Hafnium oxide thin films as a barrier against copper diffusion in solar absorbers, Sol Energ Mat Sol C 166 (2017) 140–146.
[55] B. Aguirre, R.S. Vemuri, D. Zubia, M.H. Engelhard, V. Shutthananadan, K. K. Bharathi, C.V. Ramana, Growth, microstructure and electrical properties of sputter-deposited hafnium oxide (HfO_2) thin films grown using a HfO_2 ceramic target, Appl. Surf. Sci. 257 (6) (2011) 2197–2202.
[56] N. Rochat, K. Dabertrand, V. Cosnier, S. Zoll, P. Besson, U. Weber, Infrared spectroscopy of high k thin layer by multiple internal reflection and attenuated total reflection, Phys. Status Solidi C n/a (8) (2003) 2961–2965.
[57] G. Aygun, I. Yildiz, Interfacial and structural properties of sputtered HfO_2 layers, J. Appl. Phys. 106 (1) (2009).
[58] M. Kopani, M. Mikula, E. Pinčík, H. Kobayashi, M. Takahashi, FT IR spectroscopy of nitric acid oxidation of silicon with hafnium oxide very thin layer, Appl. Surf. Sci. 301 (2014) 24–27.
[59] T.J. Bright, J.I. Watjen, Z.M. Zhang, C. Muratore, A.A. Voevodin, Optical properties of HfO_2 thin films deposited by magnetron sputtering: from the visible to the far-infrared, Thin Solid Films 520 (22) (2012) 6793–6802.
[60] C.-z. Sun, R.-d. Hong, X.-p. Chen, J.-f. Cai, Z.-y. Wu, Ultraviolet optical properties and structural characteristics of radio frequency-deposited HfO_2 thin films, Chin. J. Chem. Phys. 31 (6) (2018) 813–817.
[61] S. Rabadzhiyska, M. Ormanova, S. Valkov, N. Ivanov, P. Terziyska, K. Ivanov, P. Petrov, Study optical properties of the thin HfO_2 coatings deposited by DC reactive magnetron sputtering, J. Phys. Conf. Ser. 1859 (1) (2021) 012066.
[62] S.-S. Lin, C.-S. Liao, The hydrophobicity and optical properties of the HfO_2-deposited glass, Ceram. Int. 39 (1) (2013) 353–358.
[63] S. Lee, H. Yoon, S. Lee, S.-m. Chung, H. Kim, Investigation of the hydrophilic nature and surface energy changes of HfO_2 thin films prepared by atomic layer deposition, Vacuum 219 (2024) 112756.
[64] J. Gao, G. He, B. Deng, D.Q. Xiao, M. Liu, P. Jin, C.Y. Zheng, Z.Q. Sun, Microstructure, wettability, optical and electrical properties of HfO_2 thin films: effect of oxygen partial pressure, J. Alloys Compd. 662 (2016) 339–347.
[65] O. Kahveci, Preparation of 3-D porous pure Al electrode for Al-air battery anode and comparison of its electrochemical performance with a smooth surface electrode, ChemElectroChem 10 (20) (2023) e202300221.
[66] J. Porcayo-Calderon, R.A. Rodríguez-Díaz, E. Porcayo-Palafox, L. Martinez-Gomez, Corrosion performance of cu-based coins in artificial sweat, J Chem-Ny 2016 (1) (2016) 9542942.
[67] Z. Shen, M. An, S. Li, X. Mi, Q. Xiao, In-situ mechanical exfoliation of graphite to UV curable graphene/acrylate coatings and their corrosion resistance properties, Smart Materials and Devices 1 (1) (2025) 202401.
[68] D. Han, L. Chen, H. Jiang, W. Zhang, G. Gao, Effects of sealing treatment on the reflectivity and corrosion behavior of anodized aluminum in artificial sweat, J. Mater. Eng. Perform. (2025), https://doi.org/10.1007/s11665-025-11688-3.
[69] M. Peron, S. Cogo, M. Bjelland, A. Bin Afif, A. Dadlani, E. Greggio, F. Berto, J. Torgersen, On the evaluation of ALD TiO_2, ZrO_2 and HfO_2 coatings on corrosion and cytotoxicity performances, J. Magnesium Alloys 9 (5) (2021) 1806–1819.
[70] K. Murugan, N. Gejalakshmi, C. Kathiresan, M. Varun Karthik, K. Kamala Bharathi, Probing the ion dynamics, structural changes, and enhanced energy storage of Co3O4 thin films for aqueous zinc-ion battery applications, The Journal of Physical Chemistry Letters 16 (44) (2025) 11443–11450.
[71] K. Derkaoui, Y. Mebdoua, A. Djaibet, H. Laiche, C. Serdani, H. Lahmar, S. Benredouane, K. Boukhouidem, N. Abdelyamine, L. Samia, D.H. Hassina, T. Hadjersi, Cold-sprayed copper coatings as novel electrocatalysts for the hydrogen evolution reaction in alkaline medium, React. Kinet. Mech. Catal. (2025), https://doi.org/10.1007/s11144-025-02987-w.
[72] A.S. de Paula, B.M. Aroeira, L.H.d.O. Souza, A.C. da Cruz, M. Fedel, B.P. da Silva, F. Cotting, Influence of organic coating thickness on electrochemical impedance spectroscopy response, Coatings 14 (3) (2024) 285.